Ore Geology Reviews 140 (2022) 104567

Contents lists available at ScienceDirect

Ore Geology Reviews

journal homepage: www.elsevier.com/locate/oregeorev

Subducted sediment contributions to REE deposits recorded by alkaline mafic dikes in the Lizhuang REE deposit, Panxi area, southwest China

Ning-Bo Li [a,b,*], He-Cai Niu [a,b], Qiang Shan [a,b], Qiang Weng [a,b,c]

[a] CAS Key Laboratory of Mineralogy and Metallogeny/Guangdong Provincial Key Laboratory of Mineral Physics and Materials, Guangzhou Institute of Geochemistry, Chinese Academy of Sciences, Guangzhou 510640, China
[b] CAS Center for Excellence in Deep Earth Science, Guangzhou 510640, China
[c] University of Chinese Academy of Sciences, Beijing 100049, China

ARTICLE INFO

Keywords:
Alkaline mafic dike
Apatite
Sediment recycling
Lizhuang REE deposit
Panxi

ABSTRACT

Carbonatite-associated rare earth element (REE) deposits are the most important source of REEs worldwide. Recycled subducted sediments are critical for REE mineralization, but it remains unclear how the subducted sediments contribute to the REE mineralization. This study presents new whole-rock and apatite geochemical data for alkaline mafic dikes from the Lizhuang REE deposit, southwest China. These alkaline mafic dikes were emplaced at ca. 28.4 Ma (monazite U-Pb age), broadly coeval with the carbonatite–syenite complex and REE mineralization in the Lizhuang REE deposit. The alkaline mafic dikes have enriched Sr-Nd-Pb isotopic compositions, and variable Ba/Th and La/Sm ratios, demonstrate they were derived from an enriched mantle source, which had been modified by both slab-derived fluids and sediment melts. The apatite grains in the alkaline mafic dikes have distinctive geochemical features in their irregular cores (apatite A) and rim overgrowths (apatite B). Apatite A has low REE contents (18.6–161 ppm) and apatite B has high REE contents (1869–4288 ppm). The different REE contents in these apatites could have been caused by the addition of REE-rich carbonatitic melts at lower crustal depths. We propose that the REE-rich carbonatitic melts could be formed by melting of a sediment-rich mantle source, and that collision between India–Asia triggered the melting.

1. Introduction

Carbonatite-associated rare earth element (REE) deposits (CARDs) host>50% of the global REE resources (Weng et al. 2015). A variety of magmatic and hydrothermal processes have been proposed to explain the mineralization of CARDs (Castor, 2008; Hou et al., 2015; Jia and Liu 2020; Liu and Hou 2017; Xie et al., 2009), and a common feature of CARDs is that the REE-enriched magma is sourced from the lithospheric mantle (Hou et al., 2015; Hutchison et al., 2021). The REEs in the lithospheric mantle may have been derived from subducted sediments (Hou et al., 2015; Ling et al., 2013; Smith et al., 2016; Xue et al., 2018). Subducted sediments generally have relatively high REE contents (Plank and Langmuir, 1998) and, more importantly, recent studies have shown that some marine sediments contain significant amounts of REEs (Kato et al., 2011). Thus, tracing how subducted sediments, including carbonates, are recycled into the mantle is key for understanding REE mineralization. Mafic igneous rocks can provide insights into the nature of the mantle, and have been used to trace recycled sediments using isotopic data (e.g., Sr–Nd–Zn–B) and ratios of elements with distinct geochemical behaviors (e.g., Ba/Th, Sr/Th, and Pb/Ce; e.g., Chauvel et al., 2008; Guo et al. 2014; Labanieh et al., 2012; Yang et al. (2012)). In addition, mafic igneous rocks are generally associated with carbonatites, including at Mountain Pass, USA (Castor, 2008), Tomtor, Russia (Panina et al., 2017), Siilinjärvi, Finland (Mattsson et al., 2019), and Bayan Obo, China (Yang et al. 2011). Furthermore, a petrogenetic relationship between the carbonatites and mafic igneous rocks has been proposed in previous studies. Tappe et al. (2006) and Cooper and Paterson (2008) proposed that carbonatites can separate from lamprophyric magmas by melt immiscibility, and Castor (2008) suggested that the Mountain Pass carbonatite had a similar source as coeval mafic igneous rocks or were even derived from the mafic magmas. Poletti et al. (2016) proposed that the carbonatite and ultrapotassic rocks in Mountains Pass share a same source though there are no genetical relationship between the two rocks. Therefore, detailed studies of the mafic igneous rocks associated with

* Corresponding author at: Key Laboratory of Mineralogy and Metallogeny, Guangzhou Institute of Geochemistry, Chinese Academy of Sciences, Guangzhou 511 Kehua Street, Tianhe District, Guangzhou 510640, China.
E-mail address: liningbo@gig.ac.cn (N.-B. Li).

https://doi.org/10.1016/j.oregeorev.2021.104567
Received 8 April 2021; Received in revised form 31 October 2021; Accepted 2 November 2021
Available online 7 November 2021

REE deposits can trace the behavior of subducted sediments in the lithospheric mantle and provide new insights into CARD formation.

The Cenozoic Mianning–Dechang CARD belt is located in the Panxi area, southwest China (Fig. 1a). This belt includes the Maoniuping, Lizhuang, Muluozhai, and Dalucao REE deposits (Fig. 1b), and hosts more than 500 Mt of REE reserves. In this study, we focused on the alkaline mafic dikes in the Lizhuang REE deposit, and present whole-rock and apatite geochemical data for the alkaline mafic dikes. Based on these data, we propose that the mantle source of the alkaline mafic dikes was metasomatized by both fluids and melts, and the latter could be responsible for the REE concentrate in their source. In addition, the apatite in the alkaline mafic dikes indicate the primary magma of the alkaline mafic dikes have been mixed with REE-rich carbonatitic melts.

2. Geological background and sample descriptions

2.1. Regional geology

The Mianning–Dechang CARD belt is located in the Panxi area, along the western margin of the Yangtze Craton (Fig. 1b). These REE deposits were controlled by Cenozoic strike-slip faults and are associated with carbonatite–syenite complexes, which were generated by melting of re-fertilized lithospheric mantle (Hou et al., 2015). Zircon U–Pb ages of syenites in the deposits are 22 Ma for Maoniuping, 27 Ma for Lizhuang, 27 Ma for Muluozhai, and 12 Ma for Dalucao (Liu et al. 2015). The ages of bastnäsite (U–Pb), apatite (U–Pb), and fluorophlogopite ($^{40}Ar/^{39}Ar$) in these deposits indicate that the mineralization was coeval with the carbonatite–syenite complexes (Liu and Hou 2017; Liu et al. 2019; Weng et al., 2021a; Weng et al. 2021b). In addition, the ages of the complexes and deposits are broadly the same as the timing of deformation on the adjacent Ailao Shan–Red River shear zone (Liu et al. 2019; Wang et al., 1998), which is thought to be a deep fault zone rooted in the lithospheric mantle (Leloup et al., 1995). Extensive magmatism (i.e., lamprophyres and high-K alkaline rocks) peaked at ca. 35 Ma, is distributed along the shear zone and adjacent areas (Guo et al. 2005; Hou et al., 2006; Liu and Hou 2017; Liu et al. 2019). These igneous rocks were generated by the reactivation of the lithospheric mantle induced by the collision between India and Asia (Guo et al. 2005; Hou and Cook, 2009). From the margin to the interior of the Yangtze Craton, the potassic magmatism exhibits a systematic increase in incompatible trace element abundances, which can be explained by a progressively decreasing degree of partial melting (Guo et al. 2005).

The Lizhuang deposit is a small–medium-sized REE deposit located in the northern part of the Mianning–Dechang CARD belt (Fig. 1b). The carbonatite–syenite complex intruded metamorphosed Silurian–Triassic rocks (Fig. 1c). The REE orebodies, which are generally 30 m to 100 m long and 2 to 12 m thick, are mainly hosted in the apical fissure zones of the complex (disseminated ore) and the contact zones between intrusions and wall rocks (brecciaed ore). There are two stage of fenitization around the complex occur in the deposit, and the apatite U–Pb age from the fenites revealed that the hydrothermal alteration processes could be lasting for ~ 2 Ma (Weng et al., 2021a). Except the complex and

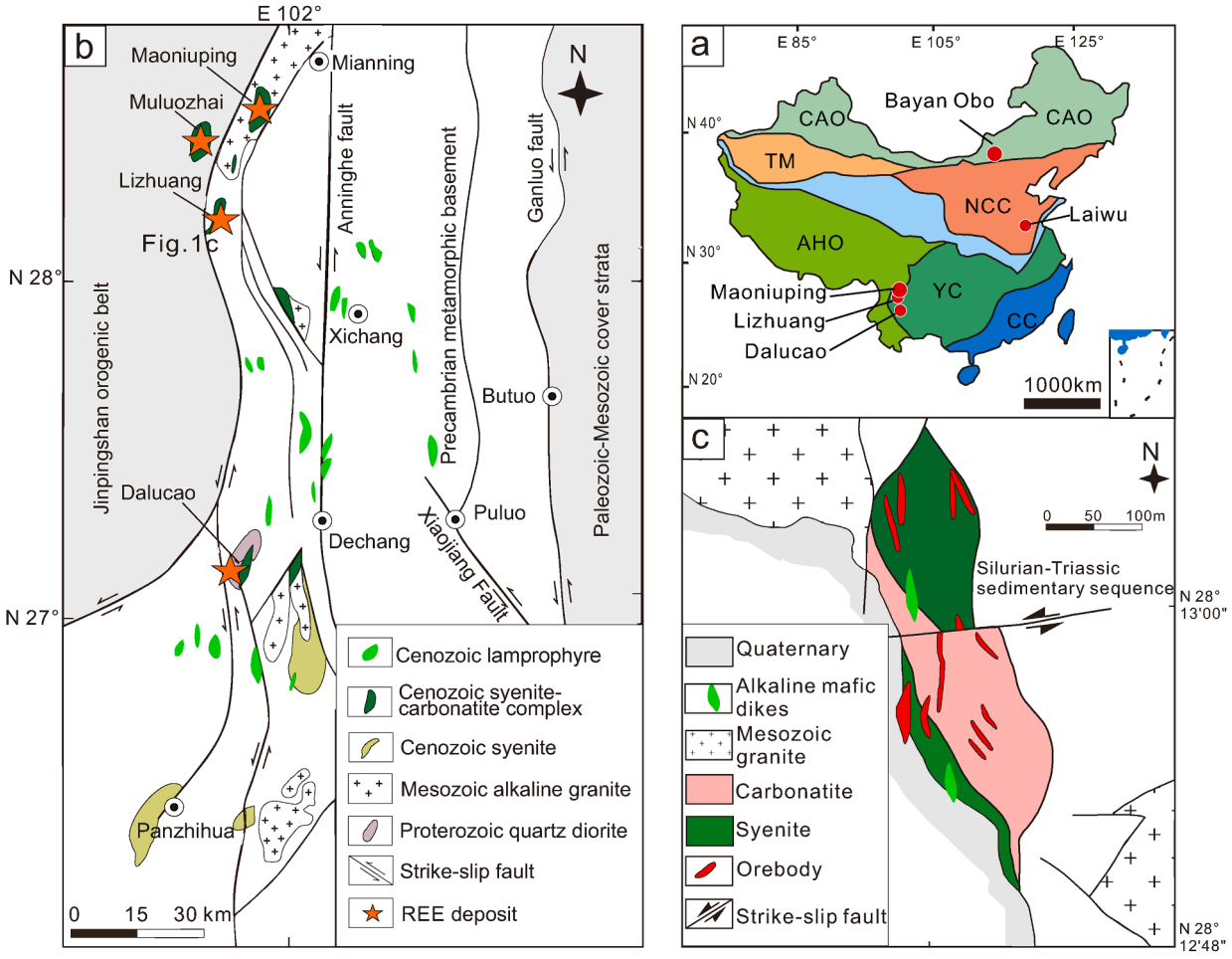

Fig. 1. (a) Schematic map showing the locations of the major CARDs in China (modified after Groves et al., 2020). CAO = Central Asian Orogen; TM = Tarim Block; NCC = North China Craton; SGO = Songpan–Ganzi Orogen; AHO = Alps–Himalayan Orogen; YC = Yangtze Craton; CC = Cathaysia Craton. (b) Sketch geological map showing the distribution of Cenozoic carbonatite–alkaline complexes and other igneous rocks (Hou et al., 2015). (c) Geological map of the Lizhuang REE deposit (modified after Tian et al., 2005).

fenites, some alkaline mafic dikes occur in the deposit and intrude the complex and orebodies (Fig. 1c and 2a).

2.2. Sample descriptions

The alkaline mafic dikes in the Lizhuang REE deposit intrude the carbonatite–syenite complex (Fig. 2a), and have variable mineralogical features. They are porphyritic texture and composed of 40–60 vol% phenocrysts, which are dominated by biotite (5–10 vol%), amphibole (50–60 vol%), and feldspar (20–30 vol%) (Fig. 2b). The groundmass is also mainly composed by biotite, amphibole and feldspar. Some of the alkaline mafic dike samples contain globular calcite ocelli (Fig. 2c). The occurrence of biotite in some of these ocelli suggests that the carbonate is magmatic in origin (Fig. 2c). In addition, calcite grains occur as inclusions in amphibole (Fig. 2d), indicating that carbonatite-rich magma could have mixed with the primary magma of the Lizhuang alkaline mafic dikes.

The accessory minerals in the Lizhuang alkaline mafic dikes include apatite, titanite, monazite, Fe–Ti oxides, and sulfides. The apatite is broadly euhedral and contains few melt inclusions and no mineral inclusions. Apatite commonly occurs as inclusions in amphibole (Fig. 2e). Cathodoluminescence (CL) images of the apatite grains reveal that they have core–rim textures and can be broadly divided into two types based on color, which are CL-dark anhedral cores (apatite A) and rims with green luminescence (apatite B; Fig. 2f).

3. Analytical methods

3.1. Monazite U–Pb dating and geochemistry

Monazite grains were handpicked from the alkaline mafic dikes under a binocular microscope. The monazite was documented using transmitted and reflected light photomicrographs, followed by cathodoluminescence (CL) imaging, in order to identify its internal structures. The geochemical composition of monazite was determined by laser ablation inductively coupled plasma mass spectrometry (LA-ICPMS) at the School of Marine Sciences, Sun Yat-sen University. Elemental contents were calculated using GLITTER 4.0 software.

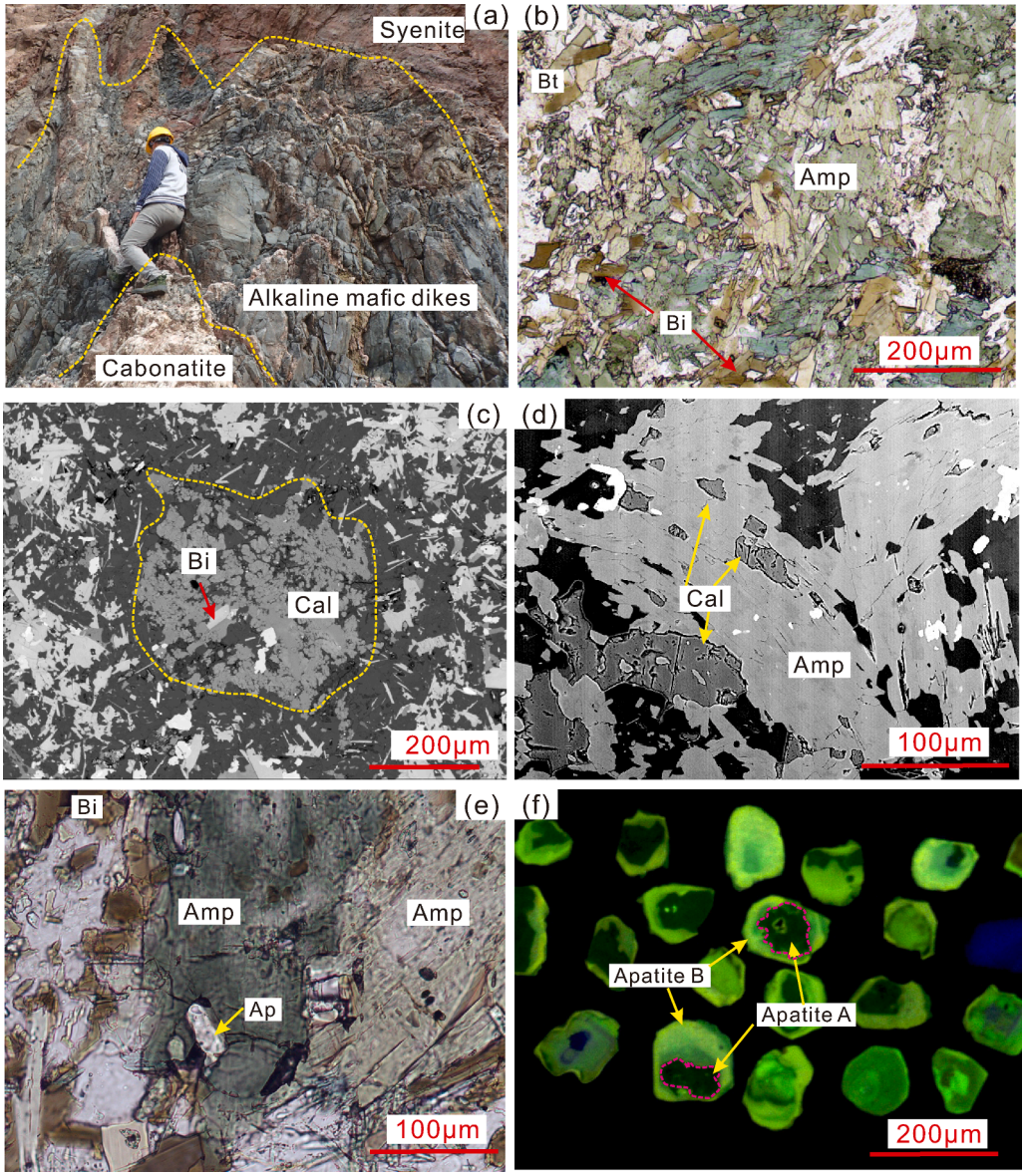

Fig. 2. (a) Field photograph showing alkaline mafic dikes intruding the carbonatite–syenite complex. (b) Microscopic image of a Lizhuang mafic dike. (b) Back-scattered electron (BSE) image showing globular calcite ocelli in the alkaline mafic dikes. (d) BSE image of calcite in amphibole. (e) Microscopic image of apatite in amphibole. (f) Color cathodoluminescence (CL) image of apatite with rim overgrowths. Bi = biotite; Amp = amphibole; Cal = calcite; Ap = apatite.

Monazite U–Pb dating was also conducted by LA-ICPMS at the CAS Key Laboratory of Mineralogy and Metallogeny, Guangzhou Institute of Geochemistry, Chinese Academy of Sciences (KLMM, GIGCAS). The Diamantina monazite standard (age = 495.26 ± 0.54 Ma; Gonçalves et al., 2018) was used as the external standard for calibration. Raw U–Pb isotopic data were processed using Iolite 4.0. Tera–Wasserburg concordia diagrams were generated with IsoplotR (Vermeesch, 2018). The LA-ICPMS operating conditions were modified from those of Kohn and Vervoort (2008).

3.2. Whole-rock geochemistry

Whole-rock major element contents were determined with an X-ray fluorescence spectrometer (Philips PW2404) at ALS Mineral/ALS Chemex (Guangzhou) Co. Ltd., Guangzhou, China. The analytical precision was better than ± 2% for most elements. Trace elements were analyzed with a Thermal Fisher iCAP RQ ICPMS equipped with a Cetac ASX-560 AutoSampler at Guizhou Tongwei Analytical Technology Co. Ltd. (GTAT). The ICP-MS procedure for trace element analysis followed the protocols of Eggins et al. (1997), with modifications described in Kamber et al. (2003) and Li et al. (2005). The trace element data have a precision of <±5%.

Whole-rock Sr–Nd–Pb isotopic ratios were also analyzed at GTAT. Sr isotopes were measured on a VG Sector 54 thermal ionization mass spectrometer, and Nd and Pb isotopes were measured on a Nu Plasma HR multiple-collector ICPMS. The detailed analytical procedures were described by Mikova and Denkova (2007) and Deniel and Pin (2001).

3.3. Mineral geochemistry

3.3.1. Major element analysis

Major element compositions of apatite and amphibole were determined with a JEOL JXA 8230 electron microprobe (EMPA) at the KLMM, GIGCAS. For apatite, the analytical conditions were: accelerating voltage of 15 kV, beam current of 20nA, and beam diameter of 5 μm. The data were processed with the ZAF correction method. The standards used were fluorapatite for Ca and P, BaF_2 for F, tugtupite for Cl, and diopside for Si. The relative precisions are ±2% for Ca, P, and F, and ±5% for Si and Cl. Xing and Wang (2017) described the analytical procedures in detail.

For amphibole, the analytical conditions were: accelerating voltage of 15 kV, beam current of 20 nA, and beam diameter of 1 μm. The standards used were orthoclase for K, albite for Na, kaersutite for Si and Al, diopside for Ca, rhodonite for Mn, rutile for Ti, magnetite for Fe, and olivine for Mg. The relative precision is ±4% for all elements.

3.3.2. Trace element analysis

Apatite trace element contents were measured with an ELEMENT XR (Thermo Fisher Scientific) sector field ICPMS coupled to a 193 nm (ArF) Resonetics RESOlution M−50 LA system at the State Key Laboratory of Isotope Geochemistry, GIGCAS. The laser conditions were as follows: beam size of 28 μm, repetition rate of 6 Hz, and energy density of ~4 J cm^{-2}. The calibration line for each element was determined by analyzing three USGS reference glasses (BCR-2G, BHVO-2G, and GSD-1G). The detailed analytical procedures and data reduction protocols were described by Zhang et al. (2019). The USGS reference glass TB-1G was measured as an unknown sample. The analytical precision (2RSD) was <±10% for most elements.

4. Results

4.1. Monazite dating

Monazite grains from sample 17LZ-06 were U–Pb dated (Tables S1–S2; Fig. 3). Fifty-five monazite grains yielded a Tera–Wasserburg U–Pb intercept age of 28.4 ± 0.1 Ma (2σ; MSWD = 4.5; common Pb was anchored at $^{207}Pb/^{206}Pb$ = 0.85, which is consistent with the whole-rock $^{207}Pb/^{206}Pb$ ratio; Fig. 3a). The monazite standard (Diamantina) does not have uniform $^{208}Pb/^{232}Th$ ratios (Gonçalves et al., 2018), and thus monazite Th–Pb ages are not presented in this study. Therefore, the monazite Tera–Wasserburg U–Pb intercept age is the best estimate of the age of the Lizhuang alkaline mafic dikes.

4.2. Whole-rock geochemistry

The whole-rock geochemical data are listed in Table S3. These samples have variable geochemical compositions, with SiO_2 = 44.18–52.84 wt%, MgO = 3.91–9.24 wt%, K_2O/Na_2O = 0.21–0.86 (except 17LZ-20 = 11). They have relatively high total alkalis contents (3.98–8.66 wt%) and belong to alkaline series in the TAS diagram (not shown). The samples have relatively low P_2O_5 contents (0.13–0.36 wt %). Primitive-mantle-normalized element diagrams exhibit negative Nb, Ta, Zr, and Hf anomalies (Table S3; Fig. 4a). The Lizhuang alkaline mafic dikes are characterized by enrichments in light REEs (LREEs) and relatively flat heavy REE (HREE) patterns ($[La/Yb]_N$ = 1.12–55.6; $[Dy/Yb]_N$ = 1.24–1.46), with negligible Eu anomalies (Fig. 4b). Sr–Nd–Pb isotope data for selected mafic dike samples are listed in Table S3 and shown in Fig. 5. The Lizhuang alkaline mafic dikes formed at < 30 Ma, and thus the measured Sr–Nd–Pb isotope ratios can be regarded as initial isotope ratios. The Lizhuang alkaline mafic dikes have radiogenic $^{87}Sr/^{86}Sr$ values (0.706911–0.710263) and low $^{143}Nd/^{144}Nd$ values (0.512528–0.512724) relative to Bulk Earth (Table S3), and elevated

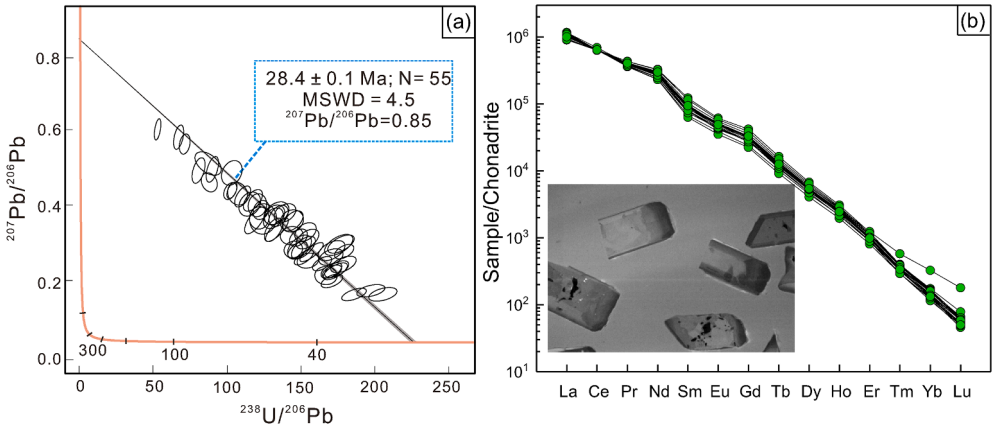

Fig. 3. (a) Tera–Wasserburg concordia diagrams and (b) chondrite-normalized REE patterns for monazite. Chondrite normalization values were taken from Sun and McDonough (1989).

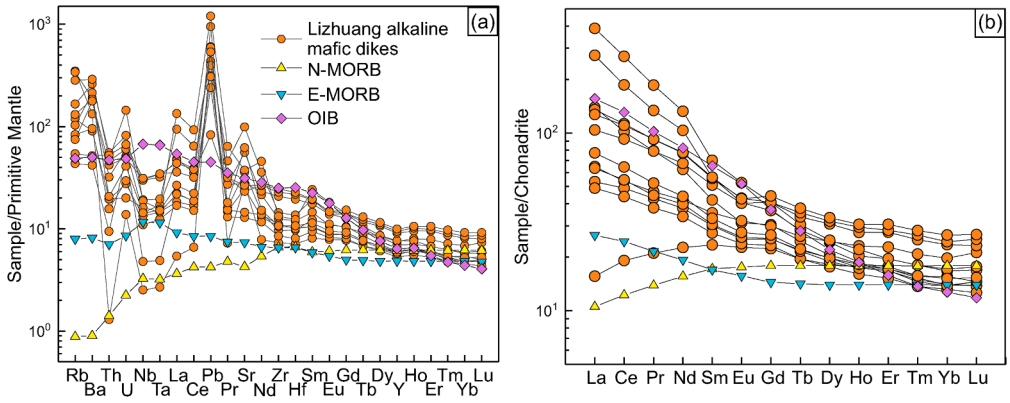

Fig. 4. (a) Primitive-mantle-normalized trace element patterns and (b) chondrite-normalized REE patterns for the Lizhuang alkaline mafic dikes. The data for N-MORB, E-MORB, and OIB were taken from Sun and McDonough (1989), and are shown for comparison. Primitive mantle and chondrite normalization values were taken from Sun and McDonough (1989).

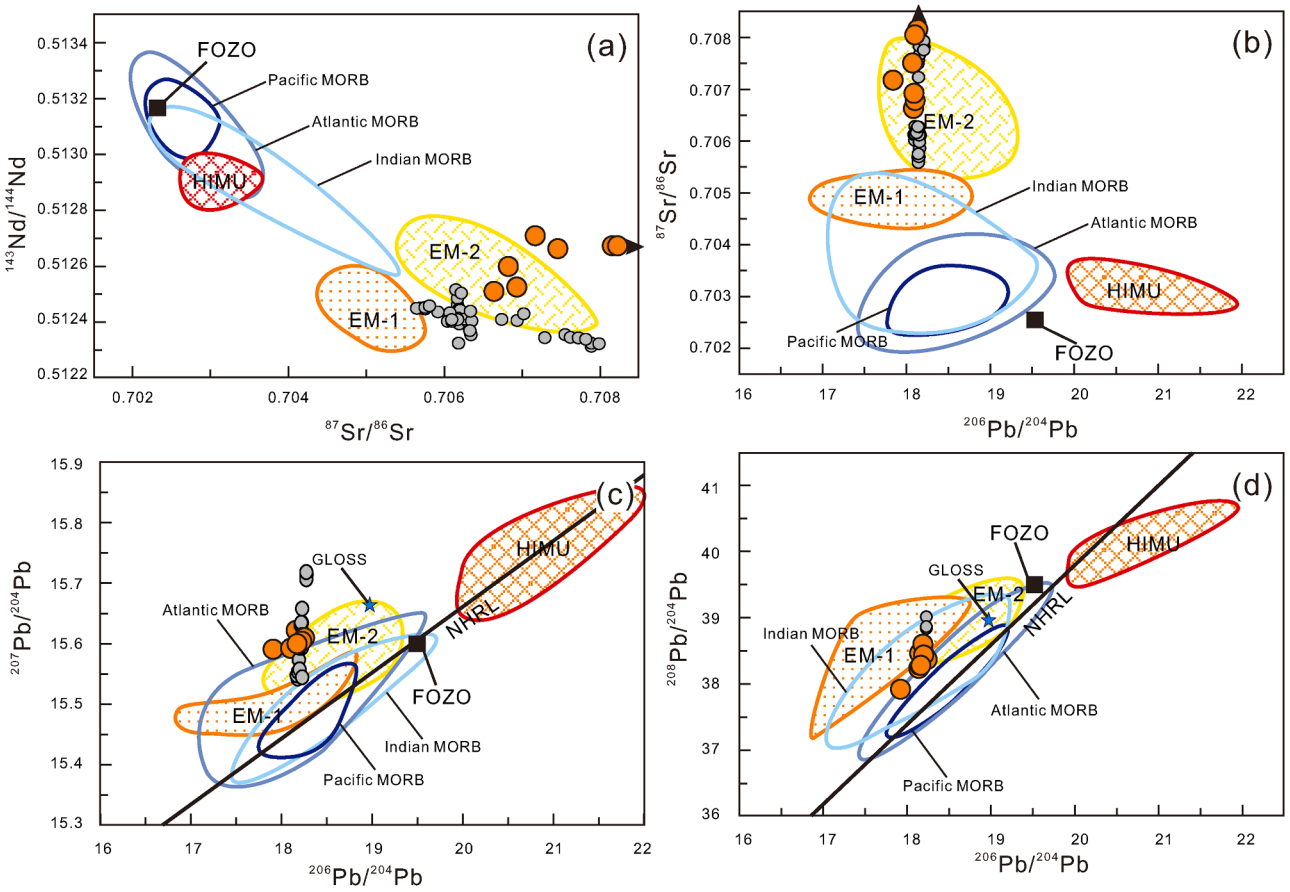

Fig. 5. Sr–Nd–Pb isotopic compositions of the Lizhuang alkaline mafic dikes. MORB, OIB, FOZO, HIMU, EM1, and EM2 data are from Hofmann (1997). The average isotopic compositions of GLOSS are from Plank and Langmuir (1998). Data for carbonatites from the Panxi area are shown for comparison.

$^{207}Pb/^{204}Pb$ (15.5866–15.6136) and $^{208}Pb/^{204}Pb$ (37.9794–38.4467) as compared with the Northern Hemisphere Reference Line (NHRL; Hart, 1984). The Lizhuang alkaline mafic dikes have similar Sr–Nd–Pb isotopic compositions as carbonatites from the Panxi area (Fig. 5).

4.3. Apatite geochemistry

Major and trace element data for apatite grains are presented in Table S4 and Fig. 6a. Apatite A and B are both fluorapatite and have similar major element compositions (Table S4), with P_2O_5 = 41.69–42.94 wt%, CaO = 53.24–55.53 wt%, and F = 2.00–3.22 wt% for apatite A, and P_2O_5 = 41.57–42.78 wt%, CaO = 52.79–55.42 wt%, and F = 2.04–2.95 wt% for apatite B. Apatite A and B have different trace element compositions, especially for Sr, Y, and REE contents (Table S4; Fig. 6a). Apatite A exhibits LREE depletion in chondrite-normalized REE patterns, with total REE contents of 18.6–161 ppm. Apatite B has convex-upward REE patterns and higher total REE contents (1870–4288 ppm) as compared with apatite A. Sr contents for apatite A and B are 1386–1953 and 1889–2227 ppm, respectively. Both apatite A and B have obviously different chondrite-normalized REE patterns as

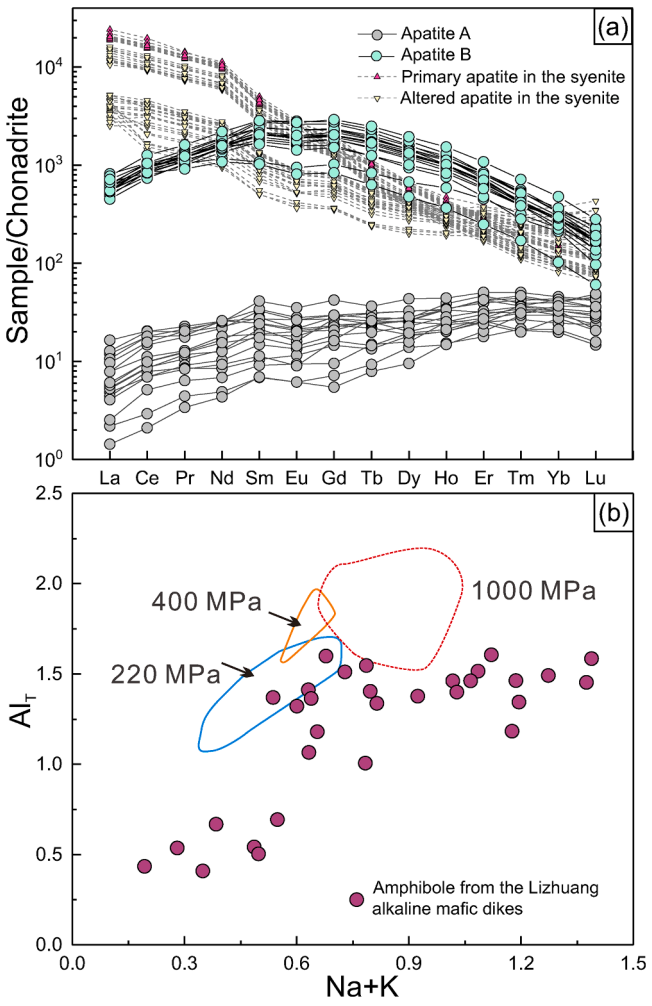

Fig. 6. (a) Chondrite-normalized rare earth element patterns for apatite from the Lizhuang alkaline mafic dikes. Data for apatite from the syenite (Weng et al., 2021a; Weng et al. 2021b) are shown for comparison. The chondrite normalization values were taken from Sun and McDonough (1989). (b) Pressure estimate diagrams for the Lizhuang alkaline mafic dikes based on the amphibole compositions (modified after Li et al. 2019).

compared with apatite from the Lizhuang syenite (Fig. 6a).

4.4. Amphibole geochemistry

Major element data for amphibole in the Lizhuang alkaline mafic dikes are listed in Table S5. All the amphibole crystals are Ca-amphiboles based on $(Ca + Na)_B > 1.0$, $Na_B < 0.50$, and $Ca_B > 1.50$. These amphiboles have Na + K = 0.19–1.39, Mg# = 0.46–0.70, and Al_T = 0.41–1.60 (Table S5). Magmatic amphibole compositional variations are typically ascribed to changes in crystallization conditions, such as pressure, temperature, and melt composition (Ribeiro et al., 2016). Previous experimental studies have shown that amphibole Al_T and Na + K values vary with pressure (Alonso-Perez et al., 2009). The amphiboles in the Lizhuang alkaline mafic dikes have variable Al_T and Na + K values, indicating that some crystallized early at pressures of > 1000 MPa (>30 km; Fig. 6b)

5. Discussion

5.1. Recycling materials recorded by the whole-rock geochemistry

Mantle-derived mafic magmas are geochemically heterogeneous due to the addition of different subducted components (Class et al., 2000; Hofmann, 1988). Radiogenic isotopic compositions are the most reliable tracers of magma sources, especially where old crustal materials or subducted sediments have been added to the mantle source. The Lizhuang alkaline mafic dikes have relatively enriched Sr–Nd–Pb isotopic compositions similar to EMII (Fig. 5), which has a geochemical signature that has been explained by addition of recycled sediments into the mantle (Jackson et al., 2007). Previous studies of dehydration and melting reactions during subduction have identified two different slab components: fluids and melts (Spandler and Pirard, 2013). These two different slab-derived components generally share similar isotopic compositions, but distinct trace element contents (Class et al., 2000). The relative immobility of some incompatible elements (e.g., Th, REE, and Nb) in aqueous fluids has been used to distinguish between metasomatizing melts and fluids (Labanieh et al., 2012). In Fig. 7a, a data compilation for melt inclusions hosted by olivine from arc settings is plotted in a Ba/Th vs. La/Sm diagram. Melt inclusions hosted by mantle minerals can be regarded as primitive arc magmas that have not undergone differentiation, such as fractional crystallization, crustal assimilation, and magma mixing. As such, the melt inclusion compositions record mantle metasomatic processes. These melt inclusions exhibit two obvious geochemical trends, including one with variable La/Sm, but uniformly low Ba/Th ratios, and another with high Ba/Th and low La/Sm ratios (Fig. 7a). The Ba/Th ratio is a proxy for the effects of aqueous fluids formed by slab dehydration, and the La/Sm ratio is a proxy for addition of sediment melts (Labanieh et al., 2012; Yang et al. (2012). Although mantle melting in the garnet stability field can produce elevated La/Sm ratios in mantle-derived mafic magmas, this process cannot change the isotopic composition. La/Sm ratios of the Lizhuang alkaline mafic dikes are clearly negatively correlated with $^{143}Nd/^{144}Nd$ values (Fig. 7b), indicative of addition of sediment melts. In addition, the Lizhuang alkaline mafic dikes have variable La/Sm (1.03–8.56) and Ba/Th (81–900; except sample 17LZ-20 with a value of 8455) ratios (Table S4; Fig. 7a). This suggests that both slab dehydration and sediment melting occurred. Such processes have been previously identified by Labanieh et al. (2012) for the Martinique arc and Class et al. (2000) for the Aleutian arc.

The depleted mantle has low Th (~0.014 ppm) and REE contents (~4.42 ppm; Salters and Stracke, 2004), but global subducting sediment (GLOSS) has relatively high Th (6.91 ppm) and REE contents (~136 ppm) (Plank and Langmuir, 1998). Recent studies have shown that some pelagic muds have high REE contents, such as in the western North Pacific Ocean (REE + Y > 5000 ppm; Kato et al., 2011; Takaya et al., 2018). Therefore, the Th and REE budget in metasomatized mantle is largely controlled by sediment recycling (e.g., Hermann and Spandler 2008; Hou et al., 2015; Plank, 2005). Furthermore, the addition of subducted sediments can make the mantle more oxidized (Kelley and Cottrell, 2009), and carbonatites and associated alkaline igneous rocks, like those associated with the REE deposits in the Panxi area, require a more oxidized mantle source than alkaline igneous complexes without carbonatites (e.g., Braunger et al., 2020). Under subduction zone conditions, elements such as large-ion lithophile (LILEs) and high-field-strength elements (HFSEs) can have enhanced solubility due to the formation of complexes in fluids (Antignano and Manning, 2008). However, HFSE, REE, and Th transport by slab-derived aqueous fluids to the mantle wedge is limited, even for supercritical fluids (Chen et al., 2018). Therefore, sediment melts are needed to enrich REEs and Th in the mantle. The total REE contents of the Lizhuang alkaline mafic dikes exhibit a positive correlation with La/Sm ratios and Th contents, which is consistent with the olivine melt inclusion data (Fig. 7c–d). As such, although both subduction-derived fluids and melts were added to the source of the Lizhuang alkaline mafic dikes, the addition of sediment melts controlled the REE enrichment.

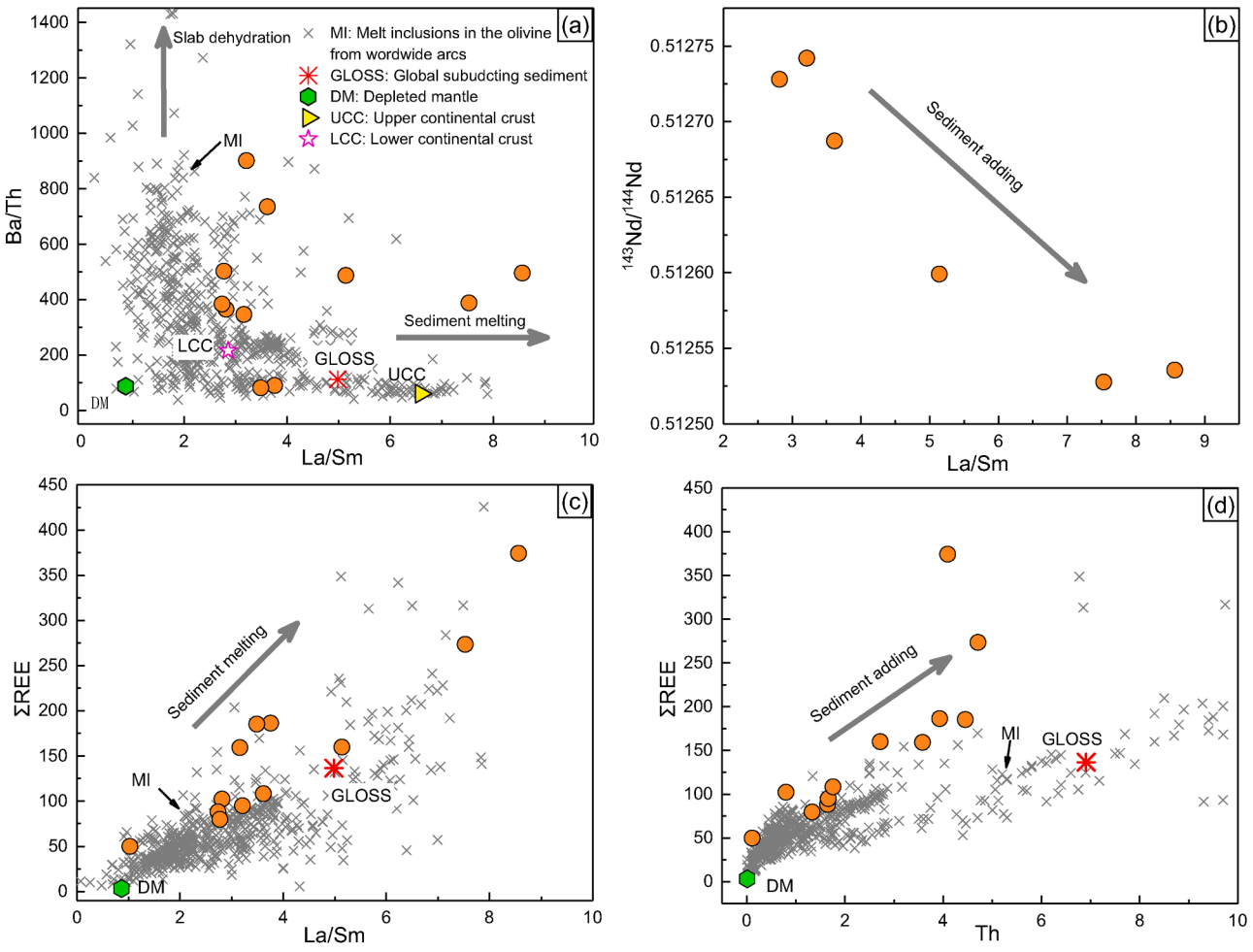

Fig. 7. Plots of (a) Ba/Th vs. La/Sm, (b) $^{143}Nd/^{144}Nd$ vs. La/Sm, (c) ∑REE vs. La/Sm, and (d) ∑REE vs. Th for the Lizhuang alkaline mafic dikes. The data compilation of melt inclusions in olivine from arcs worldwide is from Georock (http://georoc.mpch-mainz.gwdg.de/georoc/). The GLOSS data are from Plank and Langmuir (1998). DM data are from Salters and Stracke (2004). Upper continental crust (UCC) and lower continental crust (LCC) values are from Rudnick and Gao (2003).

5.2. Addition of REE-rich carbonatitic melts as recorded by apatite

Apatite occurs in nearly all igneous and metamorphic rocks, and is generally an early-crystallized mineral phase during magma evolution (Piccoli and Candela, 2002). The geochemical features of apatite are controlled by crystallization or growth conditions. Therefore, apatite can fingerprint magma evolution processes (Harlov, 2015; Qu et al., 2019). Apatite A and B in the Lizhuang alkaline mafic dikes have different geochemical features, especially with respect to REE contents (Table S4; Fig. 6a). Using compiled partition coefficients for apatite and melt ($D_{REE}^{ap/melt}$) from Cawthorn (2013), the REE patterns of the host magmas for apatite A and B were back-calculated, which are obviously

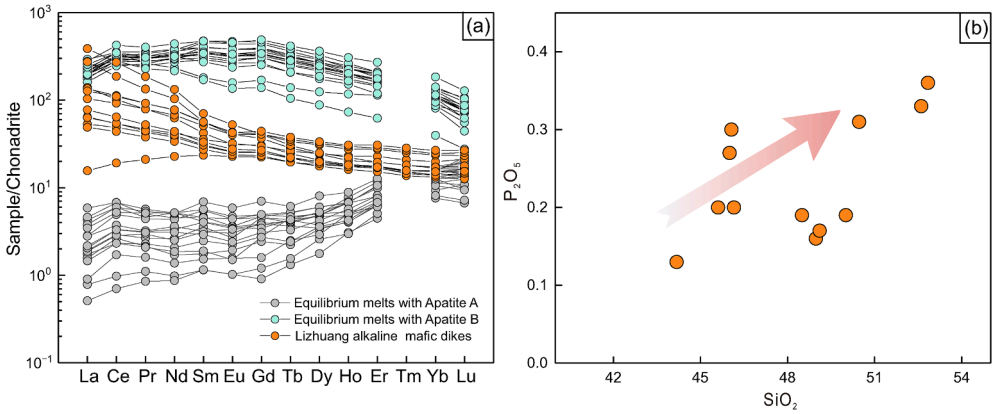

Fig. 8. (a) Chondrite-normalized REE patterns for calculated melts in equilibrium with apatite in the Lizhuang alkaline mafic dikes. Data for the Lizhuang alkaline mafic dikes are shown for comparison. Chondrite normalizing values were taken from Sun and McDonough (1989). (b) Plot of P_2O_5 vs. SiO_2 for the Lizhuang alkaline mafic dikes.

different from the Lizhuang mafic dike compositions (Fig. 8a). This indicates the apatite did not directly crystallize from the dike magmas. Apatite A has REE contents of 18.6–161 ppm and exhibits significant LREE depletion relative to the HREEs (Fig. 6a). HREE enrichment in apatite is uncommon. Previous studies of the origin and REE contents of apatite have suggested that HREE enrichment occurs during late-stage crystallization (Belousova et al., 2002; Broom-Fendley et al., 2016). Given apatite A occurs as cores, it cannot be a late-crystallizing mineral phase. The coexistence of monazite, which is a phosphate with high LREE contents, could explain the LREE depletion (Belousova et al., 2002; Harlov et al., 2002). However, the euhedral monazite (Fig. 3b) in the Lizhuang alkaline mafic dikes did not co-crystallize with the anhedral apatite A (Fig. 2f). In addition, the formation of monazite generally requires high melt REE contents (Rapp et al., 1987), but the REE contents of the host magma of apatite A were very low (Fig. 8a). Therefore, we propose that apatite A directly crystallized from a REE-poor magma that was depleted in LREEs. Apatite A is anhedral and exhibits obvious dissolution textures in their rims (Fig. 2f), implying these grains have experienced disequilibrium conditions, and that the parental magma of the dikes changed from apatite-saturated to -undersaturated conditions. Apatite saturation in a magma is mainly controlled by temperature and magmatic P_2O_5 and SiO_2 concentrations, and pressure has an insignificant control on apatite solubility (Green and Watson, 1982; Watson, 1979). The Lizhuang alkaline mafic dikes have relatively low P_2O_5 contents (0.13–0.36 wt%) and exhibit increasing P_2O_5 with increasing SiO_2 contents (Fig. 8b), which indicate apatite was not a fractionating phase during magma evolution. Therefore, fractional crystallization of apatite did not induce the change in apatite saturation. We propose that the change in apatite saturation could have been caused by the addition of REE-rich carbonatitic melts, as evidenced by: (1) the presence of magmatic calcite ocelli and calcite hosted by amphibole (Fig. 2c–d); (2) carbonatite-rich melts introducing a significant amount of REEs (Broom-Fendley et al., 2016), which could explain the high REE contents of apatite B; (3) experimental studies that have revealed apatite solubility in carbonatite-rich melts is significantly higher than for silicate melts (Hammouda et al., 2010), and thus the addition of carbonatitic melts can increase apatite saturation in a magma. Furthermore, the addition of REE-rich melts could have promoted monazite crystallization. The co-crystallization of monazite and apatite B could explain why apatite B has convex-upward REE patterns (Fig. 6a).

Some amphibole in the Lizhuang alkaline mafic dikes crystallized at high pressure (>1000 MPa; Fig. 6b), which means the REE-rich carbonatitic melts could have been added in the lower crust and formed a hybrid carbonatite-rich mafic magma (Fig. 9). In summary, the addition of sediment melts constrained by the whole-rock geochemistry of the Lizhuang alkaline mafic dikes may reflect addition of REE-rich carbonatitic melts.

5.3. *Possible origin of the REE-rich carbonatitic melts and implications for REE mineralization*

Previous studies have proposed that addition of subducted sediments to the lithospheric mantle results in REE enrichment, and is beneficial for late-stage REE mineralization (Anenburg et al., 2020; Hou et al., 2015; Ling et al., 2013; Smith et al., 2016; Xue et al., 2018). In addition, sediment-rich arc mantle typically produces magmas with high concentrations of many incompatible elements, such as REEs, as compared with sediment-starved arcs (Carter et al., 2015; Pelleter et al., 2021). Thermodynamic calculations and experimental studies suggest that sedimentary carbonate can be subducted into the deep mantle (Dasgupta and Hirschmann, 2006; Sun et al. 2020). Theoretically, sediment melts can be produced under high-pressure and -temperature conditions (Hermann and Spandler 2008), and the carbonate solidus is generally higher than the silicate solidus (Kiseeva et al., 2012; Thomson et al., 2016). For example, experimental studies of subducted pelitic sediments have revealed that hydrous silicate melt is produced at 3–4 GPa, whereas carbonatitic melts are produced at $\geq$ 5 GPa and 1050℃ (Tsuno et al., 2012). Carbonatitic melts are commonly restricted to unusually hot regimes, because the minimum temperatures for carbonatitic melts are 1020–1100℃ at 3–5 GPa (Poli, 2015).

The carbonatites in Panxi area are Ca-rich, which means they cannot have been generated from carbonated peridotite, as this source produces

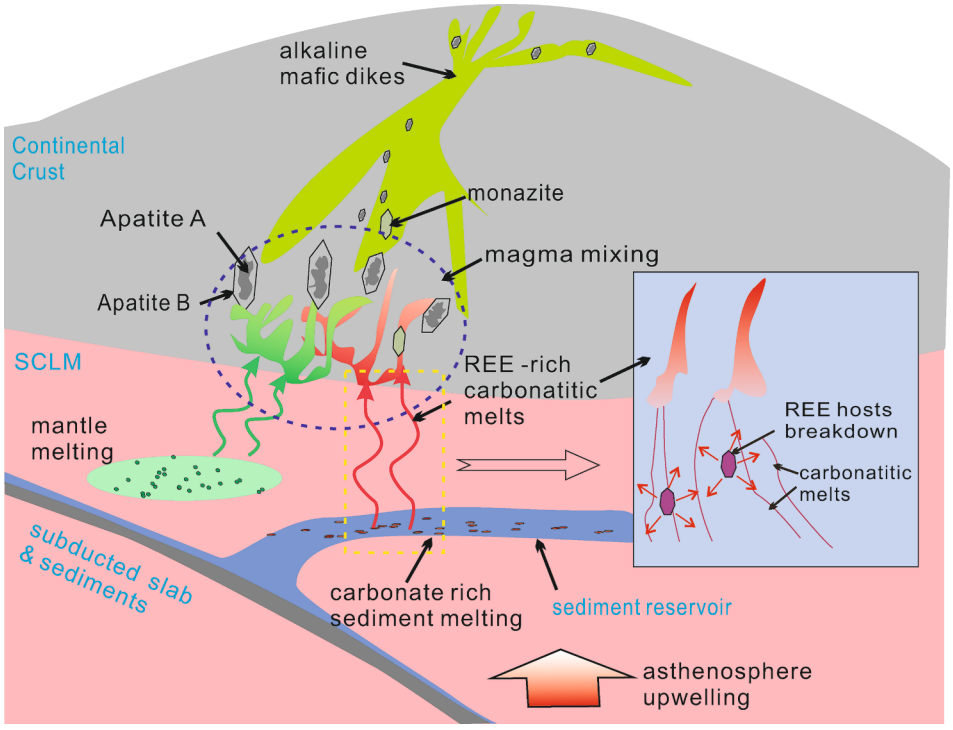

Fig. 9. Schematic petrogenetic model for the formation of the Lizhuang alkaline mafic dikes, showing sediment recycling and formation of REE-rich carbonatitic melts.

dolomitic melts (Hammouda et al., 2010). However, it is notable that only carbonated peridotite, rather than carbonate, is preserved in the deep mantle (Sun et al. 2018), and that carbonate is not the main REE carrier during subduction. Experimental studies have demonstrated that the behavior of REEs and Th are controlled by epidote (Frei et al., 2004) and allanite (Hermann, 2002), with stability temperatures of about 900℃ at 3 GPa (Carter et al., 2015) and 680–1050℃ at 2.0–4.5 GPa (Hermann, 2002), respectively. These stability conditions for epidote and allanite are not applicable to the *P–T* conditions of carbonatite melt generation. Recently, Poli (2015) proposed that water can strongly depress the solidus of carbonate and generate Ca-rich hydrous carbonatitic melts at 870–900℃. Using thermomechanical models, Currie et al. (2007) proposed that the relatively lower density of most subducted sediments results in their detachment from the subducting plate at ~ 100 km depth (~3.3 GPa), which forms a sub-horizontal sediment plume in the lithospheric mantle. Based on these studies, we propose a model for the generation of the CARDs in the Panxi area (Fig. 9). The regional mantle source was enriched by late Proterozoic and Paleozoic subduction events beneath the western Yangtze Craton (Guo et al. 2005). The two stages of subduction introduced significant amounts of sediment, including carbonate, into the mantle beneath the western Yangtze Craton (e.g., Xue et al., 2018). The collision between the India–Asia continents formed a series of Cenozoic strike-slip faults, including some *trans*-lithospheric faults, which induced asthenospheric upwelling (Hou et al., 2006). These processes caused sediment melting and generated Ca-rich hydrous carbonatitic melts. The presence of Ca-rich melts would have promoted the breakdown of allanite and epidote (e.g., Pelleter et al., 2021). The absence of the solid hosts of the REEs would have elevated the REE contents in the near-solidus partial melts (Skora et al., 2017). The hydrous carbonatitic melts then efficiently scavenged REEs from the sediments, which finally generated the REE-rich carbonatitic melts (Fig. 9).

6. Conclusions

(1) Formation of the alkaline mafic dikes in Lizhuang REE deposit involved addition of slab-derived fluids and subducted sediment melts to the mantle.

(2) Apatite in the Lizhuang alkaline mafic dikes records magma mixing with a REE-rich carbonatitic melt, which could have been formed by melting of pre-existing subducted sediments in the lithospheric mantle. The mixing may have occurred in the lower crust.

(3) Asthenospheric upwelling induced by the collision between India–Asia may have been the main factor responsible for sediment melting and formation of the REE-rich carbonatitic melts and the alkaline mafic dikes.

Declaration of Competing Interest

The authors declared that they have no conflicts of interest to this work.

Acknowledgments

We sincerely thank Prof. Huayong, Chen and Dr. Yan, Liu for handling our manuscript, and two anonymous reviewers for their constructive review comments for this manuscript. We thank Changming Xing, Dengfeng Li, Dan Wu, Le Zhang, Jinlong Ma, Neng-Ping Shen, and Xianglin Tu for their laboratory work assistance. This study was financially supported by the National Key R&D Program of China (No. 2017YFC0602301), National Natural Science Foundation of China (No. 41930424) and the Science and Technology Planning of Guangdong Province, China (NO. 2020B1212060055)

Appendix A. Supplementary data

Supplementary data to this article can be found online at https://doi.org/10.1016/j.oregeorev.2021.104567.

References:

Alonso-Perez, R., Müntener, O., Ulmer, P., 2009. Igneous garnet and amphibole fractionation in the roots of island arcs: experimental constraints on andesitic liquids. Contrib. Miner. Petrol. 157 (4), 541–558.

Anenburg, M., Mavrogenes, J.A. and Bennett, V.C. (2020) The Fluorapatite P–REE–Th Vein Deposit at Nolans Bore: Genesis by Carbonatite Metasomatism. J. Petrol. 61.

Antignano, A. and Manning, C.E. (2008) Rutile solubility in H2O, H2O–SiO2, and H2O–NaAlSi3O8 fluids at 0.7–2.0 GPa and 700–1000 °C: Implications for mobility of nominally insoluble elements. Chem. Geol. 255, 283-293.

Belousova, E.A., Griffin, W.L., O'Reilly, S.Y., Fisher, N.I., 2002. Apatite as an indicator mineral for mineral exploration: trace-element compositions and their relationship to host rock type. J. Geochem. Explor. 76 (1), 45–69.

Braunger, S., Marks, M.A.W., Wenzel, T., Chmyz, L., Guitarrari Azzone, R., Markl, G., 2020. Do carbonatites and alkaline rocks reflect variable redox conditions in their upper mantle source? Earth Planet. Sci. Lett. 533, 116041. https://doi.org/10.1016/j.epsl.2019.116041.

Broom-Fendley, S., Heaton, T., Wall, F., Gunn, G., 2016. Tracing the fluid source of heavy REE mineralisation in carbonatites using a novel method of oxygen-isotope analysis in apatite: The example of Songwe Hill, Malawi. Chem. Geol. 440, 275–287.

Carter, L.B., Skora, S., Blundy, J.D., De Hoog, J.C.M., Elliott, T., 2015. An Experimental Study of Trace Element Fluxes from Subducted Oceanic Crust. J. Petrol. 56 (8), 1585–1606.

Castor, S.B., 2008. The Mountain Pass rare-earth carbonatite and associated ultrapotassic rocks, California. Can. Mineralogist 46 (4), 779–806.

Cawthorn, R.G., 2013. Rare earth element abundances in apatite in the Bushveld Complex—A consequence of the trapped liquid shift effect. Geology 41, 603–606.

Chauvel, C., Lewin, E., Carpentier, M., Arndt, N.T. and Marini, J.-C., 2008. Role of recycled oceanic basalt and sediment in generating the Hf–Nd mantle array. Nat. Geosci. 1, 64–67.

Chen, W., Xiong, X., Wang, J., Xue, S., Li, L., Liu, X., Ding, X., Song, M., 2018. TiO2 Solubility and Nb and Ta Partitioning in Rutile-Silica-Rich Supercritical Fluid Systems: Implications for Subduction Zone Processes. J. Geophys. Res. Solid Earth 123, 4765–4782.

Class, C., Miller, D.M., Goldstein, S.L. and Langmuir, C.H. (2000) Distinguishing melt and fluid subduction components in Umnak Volcanics, Aleutian Arc. Geochemistry, Geophysics, Geosystems 1.

Cooper, A.F. and Paterson, L.A. (2008) Carbonatites from a lamprophyric dyke-swarm, South Westland, New Zealand. Can. Mineralogist 46, 753–777.

Currie, C.A., Beaumont, C., Huismans, R.S., 2007. The fate of subducted sediments: A case for backarc intrusion and underplating. Geology 35 (12), 1111. https://doi.org/10.1130/G24098A.110.1130/2007275.

Dasgupta, R., Hirschmann, M.M., 2006. Melting in the Earth's deep upper mantle caused by carbon dioxide. Nature 440 (7084), 659–662.

Deniel, C., Pin, C., 2001. Single-stage method for the simultaneous isolation of lead and strontium from silicate samples for isotopic measurements. Anal. Chim. Acta 426 (1), 95–103.

Eggins, S.M., Woodhead, J.D., Kinsley, L.P.J., Mortimer, G.E., Sylvester, P., McCulloch, M.T., Hergt, J.M., Handler, M.R., 1997. A simple method for the precise determination of ≥ 40 trace elements in geological samples by ICPMS using enriched isotope internal standardisation. Chem. Geol. 134 (4), 311–326.

Frei, D., Liebscher, A., Franz, G., Dulski, P., 2004. Trace Element Geochemistry of Epidote Minerals. Rev. Mineral. Geochem. 56 (1), 553–605.

Gonçalves, G.O., Lana, C., Scholz, R., Buick, I.S., Gerdes, A., Kamo, S.L., Corfu, F., Rubatto, D., Wiedenbeck, M., Nalini, H.A., Oliveira, L.C.A., 2018. The Diamantina Monazite: A New Low-Th Reference Material for Microanalysis. Geostand. Geoanal. Res. 42 (1), 25–47.

Green, T.H., Watson, E.B., 1982. Crystallization of Apatite in Natural Magmas under High-Pressure, Hydrous Conditions, with Particular Reference to Orogenic Rock Series. Contrib. Miner. Petrol. 79 (1), 96–105.

Groves, D.I., Santosh, M., Deng, J., Wang, Q., Yang, L., Zhang, L., 2020. A holistic model for the origin of orogenic gold deposits and its implications for exploration. Miner. Deposita 55 (2), 275–292.

Guo, F., Fan, W., Li, C., Wang, C.Y., Li, H., Zhao, L., Li, J., 2014. Hf–Nd–O isotopic evidence for melting of recycled sediments beneath the Sulu Orogen, North China. Chem. Geol. 381, 243–258.

Guo, Z., Hertogen, J., Liu, J., Pasteels, P., Boven, A., Punzalan, L., He, H., Luo, X. and Zhang, W., 2005. Potassic magmatism in western Sichuan and Yunnan provinces, SE Tibet, China: petrological and geochemical constraints on petrogenesis. J. Petrol. 46, 33–78.

Hammouda, T., Chantel, J. and Devidal, J.-L., 2010. Apatite solubility in carbonatitic liquids and trace element partitioning between apatite and carbonatite at high pressure. Geochim Cosmochim Ac 74, 7220–7235.

Harlov, D.E., 2015. Apatite: A Fingerprint for Metasomatic Processes. Elements 11 (3), 171–176.

Harlov, D.E., Andersson, U.B., Förster, H.-J., Nyström, J.O., Dulski, P., Broman, C., 2002. Apatite–monazite relations in the Kiirunavaara magnetite–apatite ore, northern Sweden. Chem. Geol. 191 (1-3), 47–72.

Hart, S.R., 1984. A large-scale isotope anomaly in the Southern Hemisphere mantle. Nature 309 (5971), 753–757.
Hermann, J., 2002. Allanite: thorium and light rare earth element carrier in subducted crust. Chem. Geol. 192 (3-4), 289–306.
Hermann, J. and Spandler, C.J., 2007. Sediment Melts at Sub-arc Depths: an Experimental Study. J. Petrol. 49, 717–740.
Hofmann, A.W. (1988) Chemical differentiation of the Earth: the relationship between mantle, continental crust, and oceanic crust. Earth Planet Sc Lett 90, 297–314.
Hofmann, A.W., 1997. Mantle geochemistry: The message from oceanic volcanism. Nature 385 (6613), 219–229.
Hou, Z., Cook, N.J., 2009. Metallogenesis of the Tibetan collisional orogen: A review and introduction to the special issue. Ore Geol. Rev. 36 (1-3), 2–24.
Hou, Z., Liu, Y., Tian, S., Yang, Z., Xie, Y., 2015. Formation of carbonatite-related giant rare-earth-element deposits by the recycling of marine sediments. Sci Rep-Uk 5 (1). https://doi.org/10.1038/srep10231.
HOU, Z., TIAN, S., YUAN, Z., XIE, Y., YIN, S., YI, L., FEI, H., YANG, Z., 2006. The Himalayan collision zone carbonatites in western Sichuan, SW China: Petrogenesis, mantle source and tectonic implication. Earth Planet. Sci. Lett. 244 (1-2), 234–250.
Hutchison, W., Finch, A.A., Borst, A.M., Marks, M.A.W., Upton, B.G.J., Zerkle, A.L., Stüeken, E.E., Boyce, A.J., 2021. Mantle sources and magma evolution in Europe's largest rare earth element belt (Gardar Province, SW Greenland): New insights from sulfur isotopes. Earth Planet. Sci. Lett. 568, 117034. https://doi.org/10.1016/j.epsl.2021.117034.
Jackson, M.G., Hart, S.R., Koppers, A.A.P., Staudigel, H., Konter, J., Blusztajn, J., Kurz, M., Russell, J.A., 2007. The return of subducted continental crust in Samoan lavas. Nature 448 (7154), 684–687.
Jia, Y.-H., Liu, Y., 2020. REE Enrichment during Magmatic-Hydrothermal Processes in Carbonatite-Related REE Deposits: A Case Study of the Weishan REE Deposit. China. Minerals 10 (1), 25. https://doi.org/10.3390/min10010025.
Kamber, B.S., Greig, A., Schoenberg, R., Collerson, K.D., 2003. A refined solution to Earth's hidden niobium: implications for evolution of continental crust and mode of core formation. Precambr. Res. 126 (3-4), 289–308.
Kato, Y., Fujinaga, K., Nakamura, K., Takaya, Y., Kitamura, K., Ohta, J., Toda, R., Nakashima, T., Iwamori, H., 2011. Deep-sea mud in the Pacific Ocean as a potential resource for rare-earth elements. Nat. Geosci. 4 (8), 535–539.
Kelley, K.A., Cottrell, E., 2009. Water and the Oxidation State of Subduction Zone Magmas. Science 325 (5940), 605–607.
Kiseeva, E.S., Yaxley, G.M., Hermann, J., Litasov, K.D., Rosenthal, A., Kamenetsky, V.S., 2012. An Experimental Study of Carbonated Eclogite at 3·5–5·5 GPa—Implications for Silicate and Carbonate Metasomatism in the Cratonic Mantle. J. Petrol. 53, 727–759.
Kohn, M.J., Vervoort, J.D., 2008. U-Th-Pb dating of monazite by single-collector ICP-MS: Pitfalls and potential. Geochem. Geophy. Geosy. 9 (4), n/a–n/a.
Labanieh, S., Chauvel, C., Germa, A. and Quidelleur, X., 2012. Martinique: a Clear Case for Sediment Melting and Slab Dehydration as a Function of Distance to the Trench. J. Petrol. 53, 2441–2464.
Leloup, P.H., Lacassin, R., Tapponnier, P., Schärer, U., Zhong, D., Liu, X., Zhang, L., Ji, S. and Trinh, P.T., 1995. The Ailao Shan-Red River shear zone (Yunnan, China), Tertiary transform boundary of Indochina. Tectonophysics 251, 3–84.
Li, B.-P., Greig, A., Zhao, J.-X., Collerson, K.D., Quan, K.-S., Meng, Y.-h., Ma, Z.-l., 2005. ICP-MS trace element analysis of Song dynasty porcelains from Ding, Jiexiu and Guantai kilns, north China. J. Archaeol. Sci. 32 (2), 251–259.
Li, N.-B., Niu, H.-C., Yang, W.-B., Lai, C.-K., Zhao, Z.-H., 2019. Orogenic Root Delamination Induced by Eclogitization of Thickened Lower Crust in the Chinese Western Tianshan: Constraints From Adakites. J. Geophys. Res. Solid Earth 124, 11089–11104.
Ling, M.-X., Liu, Y.-L., Williams, I.S., Teng, F.-Z., Yang, X.-Y., Ding, X., Wei, G.-J., Xie, L.-H., Deng, W.-F., Sun, W.-D., 2013. Formation of the world's largest REE deposit through protracted fluxing of carbonatite by subduction-derived fluids. Sci Rep-Uk 3, 1776.
Liu, Y., Chakhmouradian, A.R., Hou, Z., Song, W. and Kynický, J., 2019b. Development of REE mineralization in the giant Maoniuping deposit (Sichuan, China): insights from mineralogy, fluid inclusions, and trace-element geochemistry. Mineralium Deposita 54, 701–718.
Liu, Y., Hou, Z., 2017. A synthesis of mineralization styles with an integrated genetic model of carbonatite-syenite-hosted REE deposits in the Cenozoic Mianning-Dechang REE metallogenic belt, the eastern Tibetan Plateau, southwestern China. J. Asian Earth Sci. 137, 35–79.
Liu, Y., Hou, Z., Tian, S., Zhang, Q., Zhu, Z., Liu, J., 2015. Zircon U-Pb ages of the Mianning–Dechang syenites, Sichuan Province, southwestern China: Constraints on the giant REE mineralization belt and its regional geological setting. Ore Geol. Rev. 64, 554–568.
Mattsson, H.B., Högdahl, K., Carlsson, M., Malehmir, A., 2019. The role of mafic dykes in the petrogenesis of the Archean Siilinjärvi carbonatite complex, east-central Finland. Lithos 342-343, 468–479.
Mikova, J., Denkova, P., 2007. Modified chromatographic separation scheme for Sr and Nd isotope analysis in geological silicate samples. J. Geosci. 52, 221–226.
Panina, L., Rokosova, E.Y., Isakova, A. and Tolstov, A. (2017) Mineral composition of alkaline lamprophyres of the Tomtor massif as reflection of their genesis. Russian Geol. Geophys. 58, 887–902.
Pelleter, A.-A., Prouteau, G. and Scaillet, B., 2021. The role of sulphur on the melting of Ca-poor sediment and on trace element transfer in subduction zones: an experimental investigation. J. Petrol.
Piccoli, P.M. and Candela, P.A. (2002) Apatite in igneous systems. Rev Mineral Geochem 48, 255-292.
Plank, T., 2005. Constraints from thorium/lanthanum on sediment recycling at subduction zones and the evolution of the continents. J. Petrol. 46, 921–944.
Plank, T., Langmuir, C.H., 1998. The chemical composition of subducting sediment and its consequences for the crust and mantle. Chem. Geol. 145, 325–394.
Poletti, J.E., Cottle, J.M., Hagen-Peter, G.A., Lackey, J.S., 2016. Petrochronological Constraints on the Origin of the Mountain Pass Ultrapotassic and Carbonatite Intrusive Suite, California. J. Petrol. 57, 1555–1598.
Poli, S., 2015. Carbon mobilized at shallow depths in subduction zones by carbonatitic liquids. Nat. Geosci. 8 (8), 633–636.
Qu, P., Li, N.-B., Niu, H.-C., Yang, W.-B., Shan, Q., Zhang, Z.-Y., 2019. Zircon and apatite as tools to monitor the evolution of fractionated I-type granites from the central Great Xing'an Range. NE China. Lithos 348-349, 105207. https://doi.org/10.1016/j.lithos.2019.105207.
Rapp, R.P., Ryerson, F.J., Miller, C.F., 1987. Experimental evidence bearing on the stability of monazite during crustal anaatexis. Geophys. Res. Lett. 14 (3), 307–310.
Ribeiro, J.M., Maury, R.C., Grégoire, M., 2016. Are Adakites Slab Melts or High-pressure Fractionated Mantle Melts? J Petrol. 57 (5), 839–862.
Rudnick, R.L. and Gao, S. (2003) Composition of the continental crust.
Salters, V.J.M., Stracke, A., 2004. Composition of the depleted mantle. Geochem. Geophy. Geosy. 5 (5), n/a–n/a.
Skora, S., Freymuth, H., Blundy, J., Elliott, T., Guillong, M., 2017. An experimental study of the behaviour of cerium/molybdenum ratios during subduction: Implications for tracing the slab component in the Lesser Antilles and Mariana Arc. Geochim. Cosmochim. Ac 212, 133–155.
Smith, M.P., Moore, K., Kavecsánszki, D., Finch, A.A., Kynicky, J., Wall, F., 2016. From mantle to critical zone: A review of large and giant sized deposits of the rare earth elements. Geosci. Front. 7 (3), 315–334.
Spandler, C., Pirard, C., 2013. Element recycling from subducting slabs to arc crust: A review. Lithos 170-171, 208–223.
Sun, S.-s., McDonough, W.F., 1989. Chemical and isotopic systematics of oceanic basalts: implications for mantle composition and processes. Geolog. Soci., Lond., Spec. Publ. 42 (1), 313–345.
Sun, W.-D., Hawkesworth, C.J., Yao, C., Zhang, C.-C., Huang, R.-F., Liu, X.i., Sun, X.-L., Ireland, T., Song, M.-S., Ling, M.-X., Ding, X., Zhang, Z.-F., Fan, W.-M., Wu, Z.-Q., 2018. Carbonated mantle domains at the base of the Earth's transition zone. Chem. Geol. 478, 69–75.
Sun, Y., Hier-Majumder, S., Xu, Y., Walter, M., 2020. Stability and migration of slab-derived carbonate-rich melts above the transition zone. Earth Planet. Sci. Lett. 531, 116000. https://doi.org/10.1016/j.epsl.2019.116000.
Takaya, Y., Yasukawa, K., Kawasaki, T., Fujinaga, K., Ohta, J., Usui, Y., Nakamura, K., Kimura, J.-I., Chang, Q., Hamada, M., Dodbiba, G., Nozaki, T., Iijima, K., Morisawa, T., Kuwahara, T., Ishida, Y., Ichimura, T., Kitazume, M., Fujita, T., Kato, Y., 2018. The tremendous potential of deep-sea mud as a source of rare-earth elements. Sci. Rep.-Uk 8, 5763.
Tappe, S., Foley, S.F., Jenner, G.A., Heaman, L.M., Kjarsgaard, B.A., Romer, R.L., Stracke, A., Joyce, N. and Hoefs, J., 2006. Genesis of ultramafic lamprophyres and carbonatites at Aillik Bay, Labrador: a consequence of incipient lithospheric thinning beneath the North Atlantic craton. J. Petrol. 47, 1261–1315.
Thomson, A.R., Walter, M.J., Kohn, S.C., Brooker, R.A., 2016. Slab melting as a barrier to deep carbon subduction. Nature 529, 76-+.
Tian, S., Hou, Z., Ding, T., 2005. Geochemistry of carbonatites in Lizhuang REE deposit, Sichuan, China. Geochimica et Cosmochimica Acta Supplement 69, A256.
Tsuno, K., Dasgupta, R., Danielson, L., Righter, K., 2012. Flux of carbonate melt from deeply subducted pelitic sediments: Geophysical and geochemical implications for the source of Central American volcanic arc. Geophys. Res. Lett. 39 (16), n/a–n/a.
Vermeesch, P., 2018. IsoplotR: A free and open toolbox for geochronology. Geosci. Front. 9 (5), 1479–1493.
Wang, P.-L., Lo, C.-H., Lee, T.-Y., Chung, S.-L., Lan, C.-Y., Yem, N.T., 1998. Thermochronological evidence for the movement of the Ailao Shan Red River shear zone: A perspective from Vietnam. Geology 26 (10), 887. https://doi.org/10.1130/0091-7613(1998)026<0887:TEFTMO>2.3.CO;210.1130/9883.
Watson, E.B., 1979. Apatite saturation in basic to intermediate magmas. Geophys. Res. Lett. 6 (12), 937–940.
Weng, Q., Yang, W.-B., Niu, H.-C., Li, N.-B., Shan, Q., Fan, G.-Q., Jiang, Z.-Y., 2021a. Two discrete stages of fenitization in the Lizhuang REE deposit, SW China: Implications for REE mineralization. Ore Geol. Rev. 133, 104090. https://doi.org/10.1016/j.oregeorev.2021.104090.
Weng, Q., Yang, W.-B., Niu, H.-C., Li, N.-B., Mithchell, R.H., Zurevinske, Z., Dan, W., 2021b. Formation of the maoniuping giant REE deposit constraints from mineralogy and in suit bastnasite U-Pb geochronology. American Mineralogist In press.
Weng, Z., Jowitt, S.M., Mudd, G.M., Haque, N., 2015. A detailed assessment of global rare earth element resources: opportunities and challenges. Econ. Geol. 110 (8), 1925–1952.
Xie, Y., Hou, Z., Yin, S., Dominy, S.C., Xu, J., Tian, S., Xu, W., 2009. Continuous carbonatitic melt-fluid evolution of a REE mineralization system: Evidence from inclusions in the Maoniuping REE Deposit, Western Sichuan, China. Ore Geol. Rev. 36 (1-3), 90–105.
Xing, C.-M., Wang, C.Y., 2017. Cathodoluminescence images and trace element compositions of fluorapatite from the Hongge layered intrusion in SW China: A record of prolonged crystallization and overprinted fluid metasomatism. Am Mineral 102 (7), 1390–1401.
Xue, S., Ling, M.-X., Liu, Y.-L., Sun, W., 2018. Recycling of subducted carbonates: Formation of the Taohuala Mountain carbonatite, North China Craton. Chem. Geol. 478, 89–101.
Yang, K.-F., Fan, H.-R., Santosh, M., Hu, F.-F., Wang, K.-Y., 2011. Mesoproterozoic mafic and carbonatitic dykes from the northern margin of the North China Craton:

Implications for the final breakup of Columbia supercontinent. Tectonophysics 498 (1-4), 1–10.
Yang, W.-B., Niu, H.-C., Shan, Q., Luo, Y., Sun, W.-D., Li, C.-Y., Li, N.-B., Yu, X.-Y., 2012. Late Paleozoic calc-alkaline to shoshonitic magmatism and its geodynamic implications, Yuximolegai area, western Tianshan, Xinjiang. Gondwana Res. 22 (1), 325–340.
Zhang, L.e., Ren, Z.-Y., Xia, X.-P., Yang, Q., Hong, L.-B., Wu, D., 2019. In situ determination of trace elements in melt inclusions using laser ablation inductively coupled plasma sector field mass spectrometry. Rapid Commun. Mass Spectrom. 33 (4), 361–370.